metals

MDPI

Article

The Effect of Different Annealing Strategies on the Microstructure Development and Mechanical Response of Austempered Steels

Eliseo Hernandez-Duran [1,2,3,*], Luca Corallo [1], Tanya Ros-Yanez [4], Felipe Castro-Cerda [2,3] and Roumen H. Petrov [1,2]

1 Research Group Materials Science and Technology, Department of Electromechanical, Systems & Metal Engineering, Ghent University, Tech Lane Science Park Campus A 46, 9052 Ghent, Belgium; luca.corallo@ugent.be (L.C.); roumen.petrov@ugent.be (R.H.P.)
2 Department of Materials Science and Engineering, Delft University of Technology, Mekelweg 2, 2628 CD Delft, The Netherlands; felipe.castro@usach.cl
3 Department of Metallurgy, University of Santiago de Chile, Alameda 3363, Estación Central, 9170022 Santiago, Chile
4 CLEVELAND-CLIFFS INC, Research & Innovation Center, 6180 Research Way, Middletown, OH 45005, USA; tanya.ros@clevelandcliffs.com
* Correspondence: eliseo.hernandez@usach.cl or eliseo.hernandezduran@ugent.be

Abstract: This study focuses on the effect of non-conventional annealing strategies on the microstructure and related mechanical properties of austempered steels. Multistep thermo-cycling (TC) and ultrafast heating (UFH) annealing were carried out and compared with the outcome obtained from a conventionally annealed (CA) 0.3C-2Mn-1.5Si steel. After the annealing path, steel samples were fast cooled and isothermally treated at 400 °C employing the same parameters. It was found that TC and UFH strategies produce an equivalent level of microstructural refinement. Nevertheless, the obtained microstructure via TC has not led to an improvement in the mechanical properties in comparison with the CA steel. On the other hand, the steel grade produced via a combination of ultrafast heating annealing and austempering exhibits enhanced ductility without decreasing the strength level with respect to TC and CA, giving the best strength–ductility balance among the studied steels. The outstanding mechanical response exhibited by the UFH steel is related to the formation of heterogeneous distribution of ferrite, bainite and retained austenite in proportions 0.09–0.78–0.14. The microstructural formation after UFH is discussed in terms of chemical heterogeneities in the parent austenite.

Keywords: austempering; ultrafast heating annealing; thermo-cycling annealing

Citation: Hernandez-Duran, E.; Corallo, L.; Ros-Yanez, T.; Castro-Cerda, F.; Petrov, R.H. The Effect of Different Annealing Strategies on the Microstructure Development and Mechanical Response of Austempered Steels. *Metals* **2021**, *11*, 1041. https://doi.org/10.3390/met11071041

Academic Editors: Andrea Di Schino and Sergey V. Zherebtsov

Received: 29 April 2021
Accepted: 26 June 2021
Published: 29 June 2021

1. Introduction

A method commonly employed to achieve suitable strength–ductility balance in steels is microstructural grain refinement [1,2]. Phase transformation of austenite into micro and nanosized lath shape BCC (ferrite-martensite-bainite) sub-units can be attained via heat treatment, controlling the temperature of phase transformation [3–5]. Refinement of the parent austenite grain (PAG) size has been proved as an effective strategy towards fine-grained steel grades [2,6–8]. Among the different methods for grain refinement, the addition of microalloying elements [9] and complex thermo-mechanical treatments [10] are well-known routes to achieve a fine distribution of PAGs and improved mechanical properties in high strength steels.

On the other hand, recent trends in advanced high strength steel production account for the development of lean alloy steels with outstanding mechanical performance reached via novel and efficient heat treatments [11,12]. In order to create retained austenite containing multiphase microstructures, most of the thermo-treatments for the

new generation of steels take advantage of the decomposition of austenite and carbon partitioning from bainite and/or martensite [12]. Design and study of bainitic and martensitic based TRIP steels are mainly focused on the evaluation of results obtained by manipulation of low temperature heat treatment parameters (in the range from 200 to 500 °C), after a conventional annealing step (heating rate from 10 to 30 °C/s and soaking time at annealing temperature >60 s).

Therefore, unconventional annealing routes could be employed to modify the initial parent austenite phase, resulting in further improvement of the mechanical response of low alloy steels subjected to low temperature thermal paths. Results in thermo-cycling annealing [6–8,13] have shown that multiple annealing and cooling steps, conducing to successive martensite–austenite transformations, are an effective route to obtain a homogeneous distribution of fine-grained PAGs, starting the cycling with a coarse martensitic microstructure.

Another promising annealing route towards the new generation of steels is the ultra-fast heating (UFH) [8,14–21]. This strategy represents an optimization of the heat treatment process by employing heating rates ≥100 °C/s, reducing the annealing time from several minutes to a window of 1 to 10 s. Thanks to the development of longitudinal and transverse flux induction heating technologies, the ultrafast heating of steel strips is feasible at small and large scales [17,22,23]. Pilot-scale installations for ultrafast heating applications are reported elsewhere [22,23]. The enhanced combination of mechanical properties in lean alloyed UFH steels is developed through the formation of fine-grained heterogeneous microstructures [8,15–18,24,25]. The microstructural grain refinement reached in ultrafast heating experiments is related to several factors including (i) preferential nucleation of austenite [26,27] and interaction between ferrite recrystallization and austenite phase transformation [20,28]; (ii) pinning effect by undissolved cementite carbides [21]; (iii) restricted austenitic grain growth by the high heating rate employed [29]. Moreover, current research on this topic has confirmed that solute heterogeneities in austenite, produced due to the lack of time for homogenization during the annealing step, are responsible for the formation of a complex mixture of constituents upon cooling [15–17,24,30].

This study aims to evaluate and clarify the influence of different annealing strategies on the microstructure development and related mechanical properties of austempered bainitic steels. Annealing treatments carried out here were designed to gain insight into the influence of different microstructural characteristics, produced via modification of the initial parent austenite, on the resulting microstructures and mechanical behavior.

2. Materials and Methods

A lean low carbon steel with composition listed in Table 1 is investigated. The as-received material is a 70% cold-rolled, 1.2 mm thickness steel with a microstructure consisting of 29% of ferrite and 69 (±3)% of pearlite (Figure 1). Equally distributed bands of ferrite and pearlite were found throughout the thickness of the studied material.

Table 1. Chemical composition, wt.%.

C	Mn	Si	P	S	FE
0.28	1.91	1.44	0.009	0.005	Bal.

The as-received material was subjected to three different annealing strategies, namely conventional (CA), thermo-cycling (TC) and ultrafast heating annealing (UFH). Throughout this manuscript, the heat-treated samples will be referred as CA, TC and UFH based on their annealing history.

Cold-rolled samples of dimensions $10 \times 5 \times 1.2$ mm^3 and $90 \times 20 \times 1.2$ mm^3, with the largest axis parallel to RD, were heat-treated in a Bähr 805A/D dilatometer (TA Instruments, New Castle, DE, USA) and in a Gleeble 1500 thermo-mechanical simulator (Dynamic Systems Inc., Poestenkill, NY, USA), respectively.

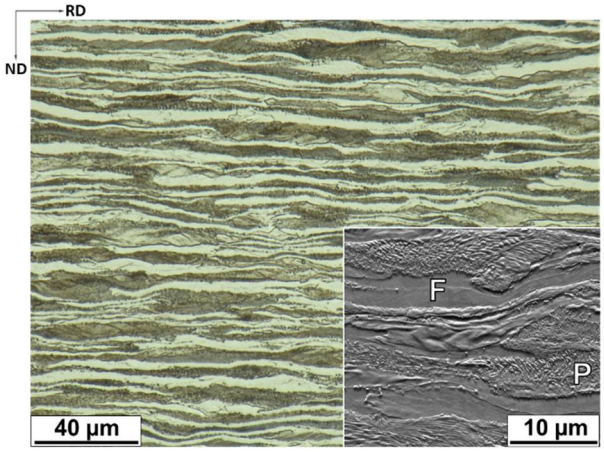

Figure 1. Microstructure of the steel in as-received 70% cold-rolled steel.

The A_{C3} temperature in each annealing treatment was estimated via dilatometric analysis employing the methodology presented in [14]. Samples treated according to the CA treatment were heated at 10 °C/s up to 885 °C, i.e., ≈30 °C above the A_{C3} (≈852 °C), and then soaked for 180 s followed by fast cooling at 160 °C/s. For TC, the first annealing step follows the same parameters as CA, and then three subsequent heating and cooling steps (cycles) were applied. The parameters of each cycle are a constant heating rate of 30 °C/s to 885 °C, soaking time of ≈2 s, and cooling at 160 °C/s to room temperature. The A_{C3} for the last annealing step (step 4) was estimated as 855 °C. The A_{C3} temperature for the samples heated at 500 °C/s in dilatometer was estimated as 892 °C. Nevertheless, this value was obtained in samples heated at 500 °C/s up to the A_{C1} temperature (767 °C), then the heating rate declined to ≈380 °C/s due to the decrease in efficiency of the longitudinal flux induction heating in dilatometer above the curie point and by the formation of paramagnetic austenite. Previous evaluations of the A_{C3} evolution with the heating rate in cold-rolled low alloy steels [31,32] indicated that the A_{C3} temperature shifts slightly when high heating rates are applied. Thomas [31] reported a shift of 1 to 3 °C of the A_{C3} temperature by increasing the heating rate from 100 °C/s to 1000 °C/s in 1020, 1019M and 15B25 cold-rolled steels. Using the Gleeble simulator, UFH samples were heated at 500 °C/s up to 925 °C, approximately 30 °C above the A_{C3} estimated by dilatometric analysis. Then, an isothermal holding step not greater than 0.3 s was employed to avoid chemical homogenization and austenitic grain growth at the annealing temperature. The selected cooling rate, after the annealing step, was 160 °C/s.

Figure 2a,b show the dilatometric curves for CA and TC obtained in samples directly cooled to room temperature and in samples isothermally held at 400 °C. The formation of martensite is clear from the expansion observed below the $M_s^{5\%}$ temperature in the dilatation-change in length v/s temperature curves (Figure 2a,b). In this work, the $M_s^{5\%}$ was defined as the temperature at which a 5% of the total dilatation generated by the martensitic transformation was measured by applying the lever rule method. Since it was not possible to reach a constant heating rate of 500 °C/s in the dilatometer, the M_S temperature for the sample peak annealed at 500 °C/s to 925 °C (UFH) was estimated by means of numerical differentiation of the cooling curves recorded in samples heat-treated using the Gleeble simulator. Figure 2c presents the change in the slope of the cooling curve at low temperature due to the exothermic characteristics of the austenite to martensite transformation. The insert in Figure 2c displays the derivate of the cooling curve.

M_S temperatures of 346 (±5) °C, 322 (±4) °C and 346 (±8) °C were estimated for CA, TC and UFH, respectively. The values presented in parenthesis correspond to the standard deviation of at least 2 measurements. These experimental results are in good agreement with the calculated M_S of 335 °C [33]:

$$\mathrm{M_s(^\circ C)} = 692 - 502\mathrm{C}^{0.5} - 37\mathrm{Mn} - 14\mathrm{Si}\ (\mathrm{wt.\%}) \quad (1)$$

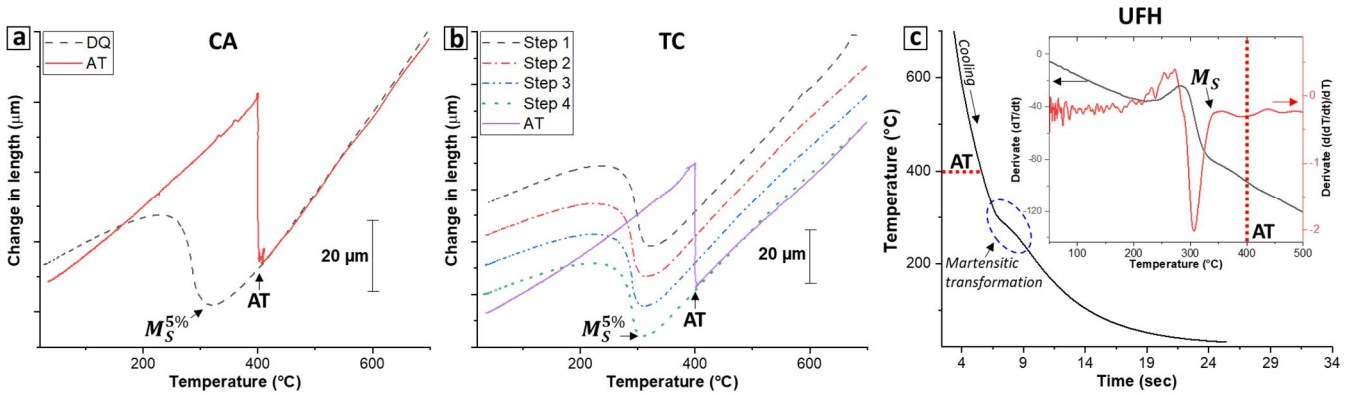

Figure 2. Dilatometric curves obtained during the cooling step, i.e., after the annealing treatments for samples (**a**) CA and (**b**) TC. (**c**) Temperature profile obtained during cooling for the ultrafast heated sample; the insert in (**c**) shows the estimation of the M_S temperature via differentiation of the recorded cooling curve.

On the other hand, the dilatation measured during the isothermal step at 400 °C is to a large extent generated by the transformation of austenite to bainite (Figure 2a,b). Based on the dilatometric results, a set of samples were subjected fast cooling and isothermal at 400 °C for 600 s to induce the stabilization of austenite via carbon redistribution during bainite formation [34]. The austempering process (AT) was performed at 400 °C to avoid the formation of martensite upon cooling. In this way, the analyses of competitive reactions typically observed in Q&P steels [35] such as carbon partitioning from martensite to austenite and/or the tempering of martensite during the isothermal step are excluded in this work.

Figure 3a,b display the temperature record of samples heat-treated in the Gleeble thermomechanical simulator. The temperature was controlled using a K-type thermocouple spot welded to the geometrical center of each sample. Additionally, extra thermocouples were welded at different locations of the sample for measuring possible thermal gradients close to the control thermocouple. Depending on the experimental setup, a small homogeneously treated zone can be obtained in samples heated by Joule effect (electric resistance heating) in the Gleeble simulator. Then, to determine the size of this zone, Vickers hardness measurements were made along the RD direction, on the ND plane. A homogeneous zone of at least 12 mm was determined by employing this method. As schematically presented in Figure 3c, samples used for microstructural and mechanical characterization were extracted from the homogeneously treated zone, which is enclosed by dashed lines. Figure 3c also presents the sample geometry used for tensile testing. Note that the gauge length and shoulders of the dog bone sample fall within the homogeneously treated zone.

The microstructures were characterized by means of light optical microscopy (LOM), scanning electron microscopy in secondary electron mode (SE) and electron backscattered diffraction (EBSD). Samples for microstructural characterization were extracted from the region next to the reduced section of the tensile samples. Metallographic examinations were performed on the RD-ND plane (see Figure 3d). Samples were prepared by grinding and polishing to 0.04 μm colloidal silica suspension (OP-U). LOM micrographs, SE images and EBSD scans were acquired at 280 μm from the sample surface. Image analyses via LOM and SE mode were carried out in samples pre-etched with Nital 2% (2 vol.% HNO_3 in ethanol). A scanning electron microscope FEI Quanta 450 FEG-SEM (ThermoFisher, Hillsboro, OR, USA) was used for microstructural characterization. SE images were acquired employing a working distance of 10 mm and an acceleration voltage of 15 kV. EBSD patterns were acquired using pixels with a hexagonal grid, step size of 120 nm, acceleration voltage of 20 kV, working distance of 14 mm and sample pretilt of 70°. EBSD data acquisition and detector control were operated with EDAX-TSL OIM Data Collection v7.3 software (EDAX AMETEK BV, Tilburg, The Netherlands). The acquired data were post-processed using TSL

OIM Analysis v7 software. The minimum grain size was defined as 5 pixels per grain and grain misorientation angle of 5°.

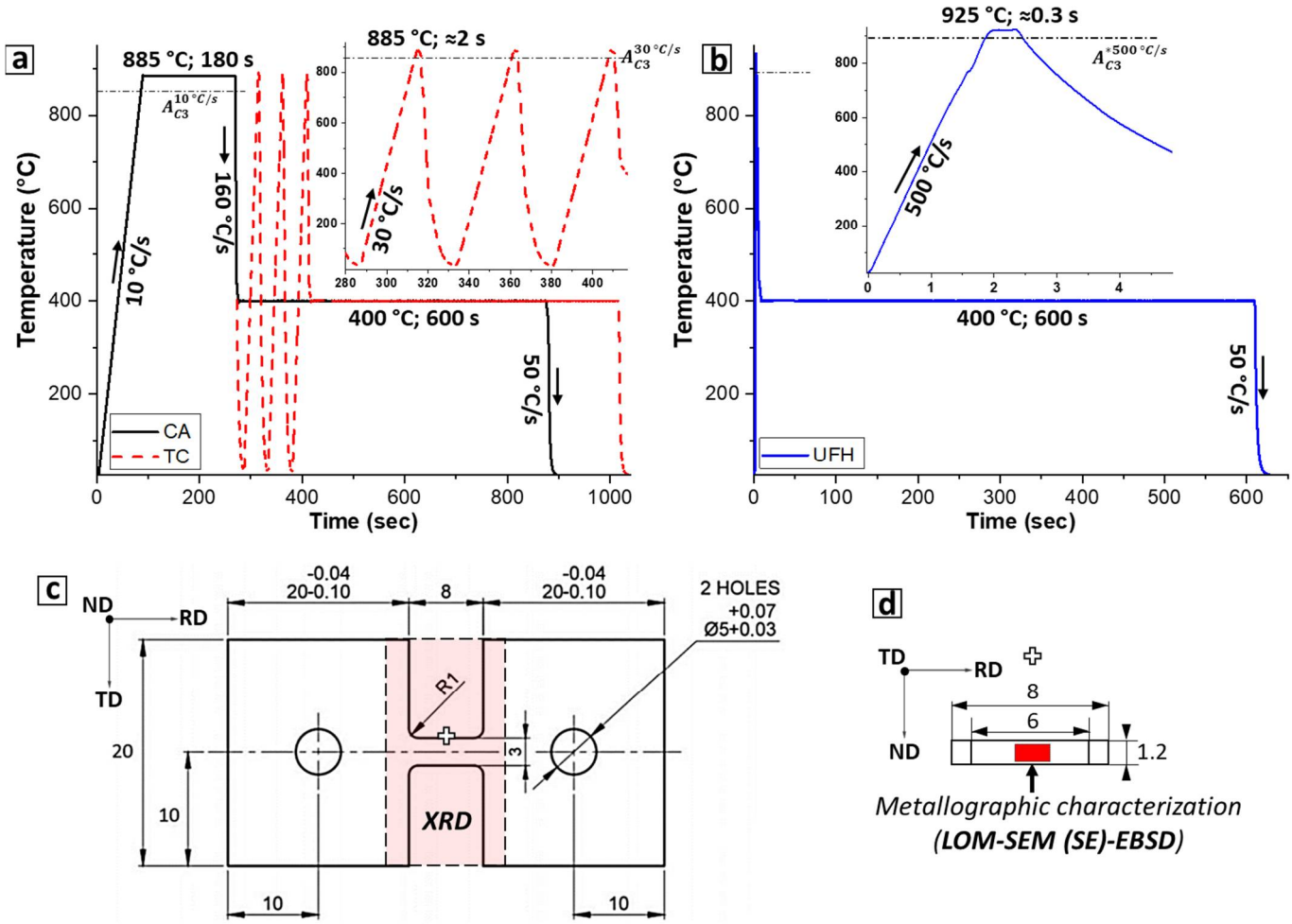

Figure 3. Record of the thermal treatments carried out in the Gleeble simulator: (**a**) CA and TC samples; (**b**) UFH sample. The inserts in (**a**) and (**b**) show the actual temperature recording for the TC and UFH samples, before the austempering step. Horizontal dotted lines denote the A_{C3} temperatures estimated by dilatometry. (**c**) Dog bone geometry and (**d**) area used microstructural characterizations (dimensions in mm). The area enclosed by dashed lines indicates the homogenously heat-treated zone obtained in samples treated using the Gleeble simulator. The cross next to the central region of the gauge length indicates the area used for metallographic characterization.

Taking advantage of the orientation relationship between bainite and parent austenite [36], parent austenite grains (PAGs) were reconstructed from the measured EBSD data using the computer code developed by Gomes et al. [37]. PAG definition was based on 7 square pixels per grain domain and misorientation of 15°.

Quantification of the amount retained austenite (RA) and the carbon content of austenite were estimated by means of X-ray diffraction (XRD) measurements in a Siemens Kristalloflex D5000 diffractometer (Mo-kα source, operation parameters: 40 kV and 40 mA) (Brücker Belgium SA/NV, Kontich, Belgium). Samples cut from the homogenously treated zone were prepared on the RD-TD plane, which is the plane normal to the ND direction (see Figure 3c). A surface layer of ≈300 μm was removed by grinding, followed by repeated polishing and etching steps. XRD patterns were acquired in the 2θ range from 25° to 45° using a step size of 0.03°, dwell time of 20 s and sample holder rotation of 15 rpm. The volume fraction of austenite was determined by the direct comparison method [37] using the integrated area of the $(200)^{BCC}$, $(211)^{BCC}$, $(220)^{FCC}$ and $(311)^{FCC}$

peaks. The retained austenite carbon content was calculated based on the relationship proposed by Roberts [38]:

$$a_\gamma = 3.548 + 0.044C_\gamma \quad (2)$$

where a_γ is the lattice parameter (in Å) and C_γ is the austenite carbon content (in wt.%).

Tensile tests were performed in an Instron 5000 device (Instron, Boechout, Belgium) imposing a strain rate of 0.001 s^{-1}. Subsize tensile samples of geometry presented in Figure 3c were strained at constant strain rate up to fracture. Two samples were tested for each austempered condition. The strain evolution during testing was locally measured by 2D-digital image correlation. Image analysis and data evaluation were processed with the Match ID software (Version 2018, MatchID, Ghent, Belgium). An initial gauge length of 6 mm was digitally defined for the strain calculations. Reported yield strength values were based on the 0.2% engineering strain offset. Absorbed energy during uniaxial tensile deformation was calculated as the integrated area under the engineering stress–strain curves. Strain hardening rate was determined as the first derivative of the true stress with respect to the true strain evolution up to necking. Before differentiation of the true stress v/s true strain values, the acquired data points were smoothed using the Locally Weighted Scatterplot Smoothing method (LOWESS).

3. Results

3.1. Microstructure

To evaluate whether ferrite was formed upon cooling, after the annealing steps, an initial microstructural characterization was performed by means of SEM analysis on directly quenched samples (Figure 4). The microstructure of direct quench samples consists predominantly of a lath martensitic (M) matrix, and allotriomorphic ferritic (F) grains are also distinguished (dark gray grains in Figure 4). Ferritic grains of about ≈ 1 μm size are observed at parent austenite grain boundaries in CA (Figure 4a) and TC (Figure 4b,e). Widmanstätten ferrite plates (F_W) [38] were also detected in CA (Figure 4d). A ferrite fraction lower than 1% was obtained after fast cooling for CA, while 2.5 (±0.5)% of ferrite was quantified for TC. The UFH sample mainly consists of martensite and 8.5 (±0.4)% of ferrite with an average grain size of 1.2 (±0.5) μm (Figure 4c). Regions with undissolved spheroidized and lamellar cementite particles (θ) are presented in Figure 4f.

Microstructures produced via a combination of the different annealing strategies and austempering at 400 °C are shown in Figure 5. Inverse pole figures (IPF) for the reconstructed PAGs are presented in Figure 5a–c. The middle row of images (Figure 5d–f) shows combined EBSD image quality and phase maps, where retained austenite grains of film (γ_F) and blocky-type (γ_B) morphologies, are highlighted in green. Bainite and ferrite appear light red. Dark-red to black constituents observed by the image quality (IQ)-phase maps presumably correspond to martensite (M), produced by austenite transformation during the final cooling step [39], after the isothermal holding at 400 °C. The lattice distortion and high dislocation density in martensite decrease the diffraction pattern quality, resulting in a lower and darker IQ scale value than the obtained for the bainitic matrix [39,40]. Based on EBSD-IQ quantification, the amount of martensite was not greater than 1% for all austempered samples. Grain boundaries of misorientation angle between 5–15° and 15–65° are indicated by white and black lines, respectively. TC and UFH annealing led to finer bainitic blocks than those obtained under conventional annealing (see the bainitic block length distribution in Figure 6a). The third row of figures (Figure 5g–i) displays the secondary electron micrographs of the austempered steel grades. A set of parallel bainitic blocks and films of retained austenite are observed in the CA sample (Figure 5g). As presented in the EBSD maps, finer microstructures resulted for the steel samples processed via TC and UFH (Figure 5h,i). Islands with a less etched appearance correspond to partially austenitic–martensitic constituents (M/γ) [39]. Those constituents are clearly distinguished in the EBSD IQ-Phase maps, where M is surrounded by retained austenite grains (Figure 5d–f). The formation of M upon the final cooling step arises due to

the heterogeneous distribution of carbon in the residual austenite after bainite transformation during austempering [41–43]. In Figure 5i, undissolved carbides (θ) are also distinguished.

The amount of retained austenite in austempered samples was quantified via XRD as 14%, 15.3%, and 13.8% for the samples CA, TC and UFH, respectively (Table 2). A slightly lower fraction of RA was quantified via EBSD; this is related to non-indexed RA grains with a size smaller than the step size employed for the EBSD data acquisition [18,44].

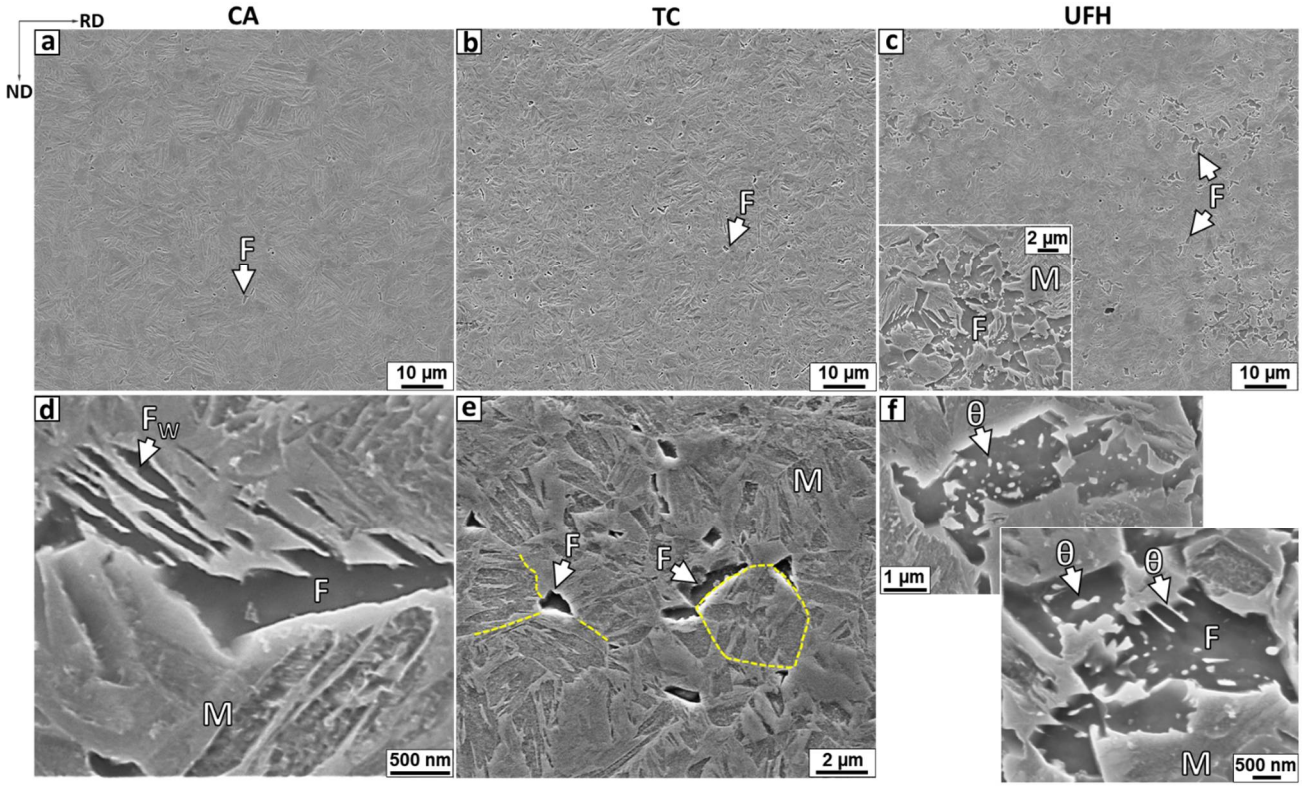

Figure 4. Microstructures of samples directly cooled to room temperature after the annealing step. (**a**–**d**) CA, (**b**–**e**) TC and (**c**–**f**) UFH. In (**e**), prior austenite grain boundaries are highlighted by dashed lines. M: Martensite; F: Ferrite; F_W: Widmanstätten ferrite; θ: Undissolved cementite particles.

The grain size distributions for the austempered steels are presented in Figure 6. A marginal difference and equivalent grain distributions were found for samples treated via TC and UFH, while the conventional annealed steel shows larger bainitic blocks and PAGs. Average bainitic block lengths of 5.3 µm, 3.5 µm and 3.4 µm were obtained for samples CA, TC and UFH, respectively (Figure 6a). PAG reconstructions also revealed that thermo-cycling and ultrafast heating annealing led to grain refinement of the parent austenite and similar grain distributions were obtained after these unconventional types of annealing strategies. Additionally, the narrow distribution of PAGs obtained after TC and UFH is an indication of a more homogeneous distribution of grains (Figure 6b). The average reconstructed PAG sizes for samples CA, TC and UFH are 8.6 µm, 5.7 µm and 5.5 µm, respectively.

Both grain major axis and grain aspect ratio (minimum grain length/maximum grain length) distributions in RA are not greatly influenced by the prior annealing treatment. An average RA grain major axis between 1.5 µm and 1.8 µm was produced after the combination of the different annealing strategies and subsequent austempering (Figure 6c), with the largest distribution of grains for CA. Measured RA grain aspect ratio values display normal distributions with maximum and average close to 0.4, which is related to a rather elongated RA grain shape (Figure 6d).

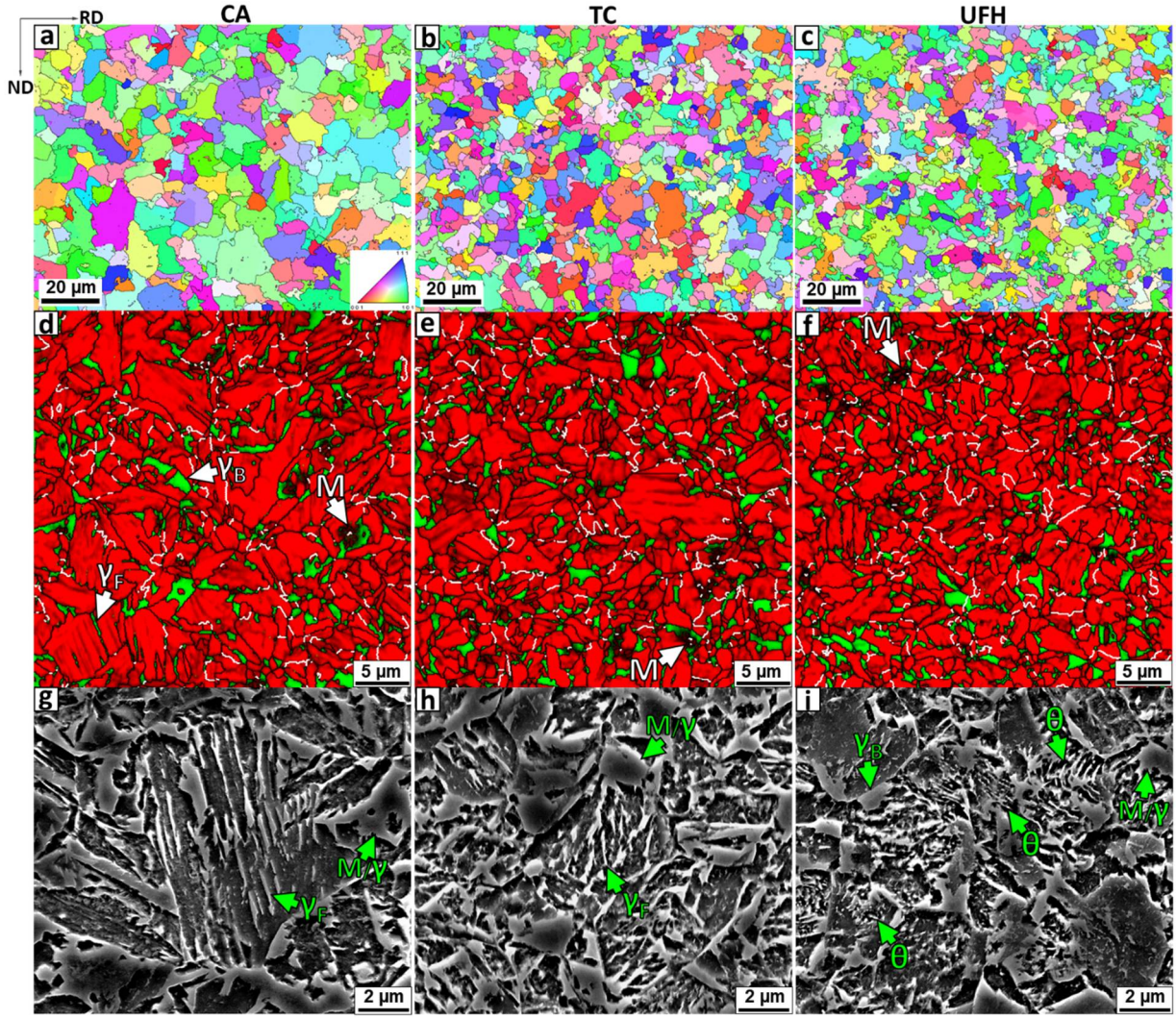

Figure 5. (**a**,**d**,**g**) CA, (**b**,**e**,**h**) TC and (**c**,**f**,**i**) UFH. Microstructures obtained after isothermal holding at 400 °C for 600 s: The first row of images presents the inverse pole figure of the reconstructed PAGs. EBDS IQ-Phase maps and secondary electron images are shown in the second and third row of images, respectively. Retained austenite grains (FCC) appear highlighted in green in the combined IQ-Phase maps, while bainite, ferrite and martensite appear red. White and black lines delineate boundaries of misorientation angle between 5–15° and 15–63°, respectively. M: Martensite; γ: Retained austenite of film (γ_F) and blocky-type (γ_B) morphologies. M/γ: martensite-retained austenite constituent; θ: undissolved cementite particles. Note that the magnification increases from the first to the third row of images.

Table 2. Microconstituents quantification (standard deviation).

Sample	Bainite,% *	Ferrite (SEM),%	Martensite (EBSD), %	RA (EBSD), % (0.2)	RA (XRD), % (0.5)	RA Carbon Content (XRD), wt.%
CA	85.0 (0.5)	<1	<1	11.9	14.0	1.36 (0.02)
TC	82.2 (0.7)	2.5 (0.5)	<1	12.5	15.3	1.33 (0.02)
UFH	77.7 (0.7)	8.5 (0.4)	<1	12.3	13.8	1.40 (0.01)

* Note: Bainite = 100-Ferrite$^{(SEM)}$-Martensite$^{(EBSD)}$-RA$^{(XRD)}$.

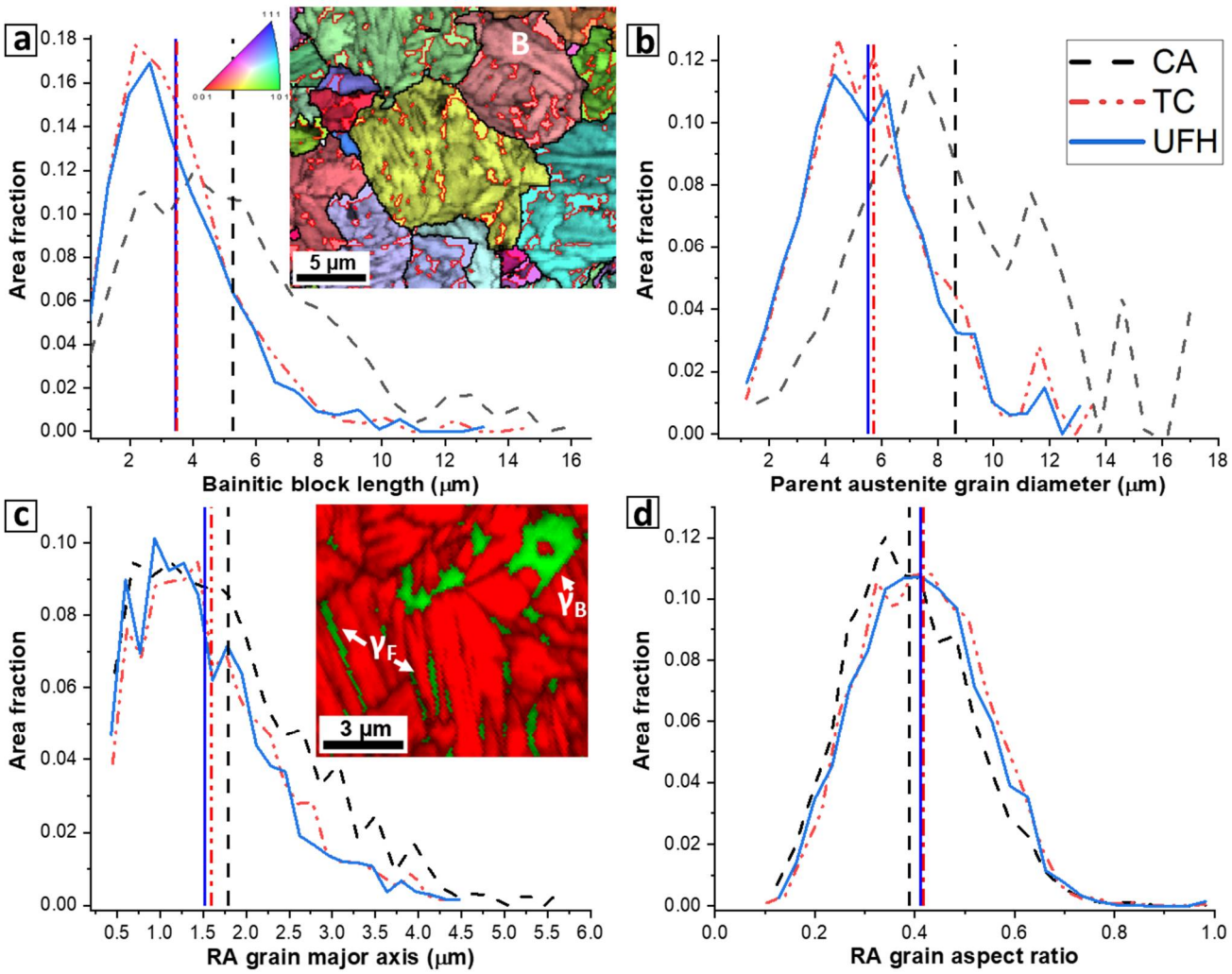

Figure 6. Grain size distribution: (**a**) bainitic block length. (**b**) reconstructed parent austenite grain size diameter. (**c**) retained austenite grain diameter. (**d**) retained austenite grain aspect ratio. Vertical lines denote the average value for each distribution. In (**a**), an IPF of reconstructed PAGs is presented together with the respective IQ map of the "child" bainitic blocks (B) formed after austempering for the CA sample. Retained austenite grains are enclosed by red boundaries. Film (γ_F) and blocky-like (γ_B) RA grains are highlighted in (**c**).

3.2. Textures

Texture analysis was carried out to elucidate the influence of the different annealing strategies on the crystallographic orientation of the transformation products in the studied steels. Figure 7 presents the orientation distribution functions (ODF) for the as-received cold-rolled material and austempered steels. BCC texture is presented at $\varphi_2 = 45°$ section of the Euler space and the main texture components of rolled BCC-Iron (Figure 7a) are presented for comparison. The as-received material (CR) shows a strong ND-RD texture which is typical for cold-rolled ferritic steels [36] and the rotated cube component {001}<110> (Figure 7b). After conventional annealing (Figure 7c), the RD texture fiber disappeared and high intensity is observed along with the ND fiber, with local maxima of orientations concentrated close to the {554}<225> and {111}<112> texture components. Thermo-cycling led to a maximum intensity of 1.64 multiples of random distribution (mrd) (Figure 7d). High intensity is observed close to ND ({554}<225>; {111}<112>) and RD ({112}<110>; {113}<110>) texture components. {001}<110> components are also distinguished after thermo-cycling. Texture obtained after UFH resembles the cold-rolled texture with a strong RD-ND type of texture (Figure 7e). The convex curvature of the ND fiber in the CR sample is maintained

in the ultrafast heated bainitic steel. At the same time, the intensity for RD-ND fibers and {001}<110> texture components is lower than that observed in CR.

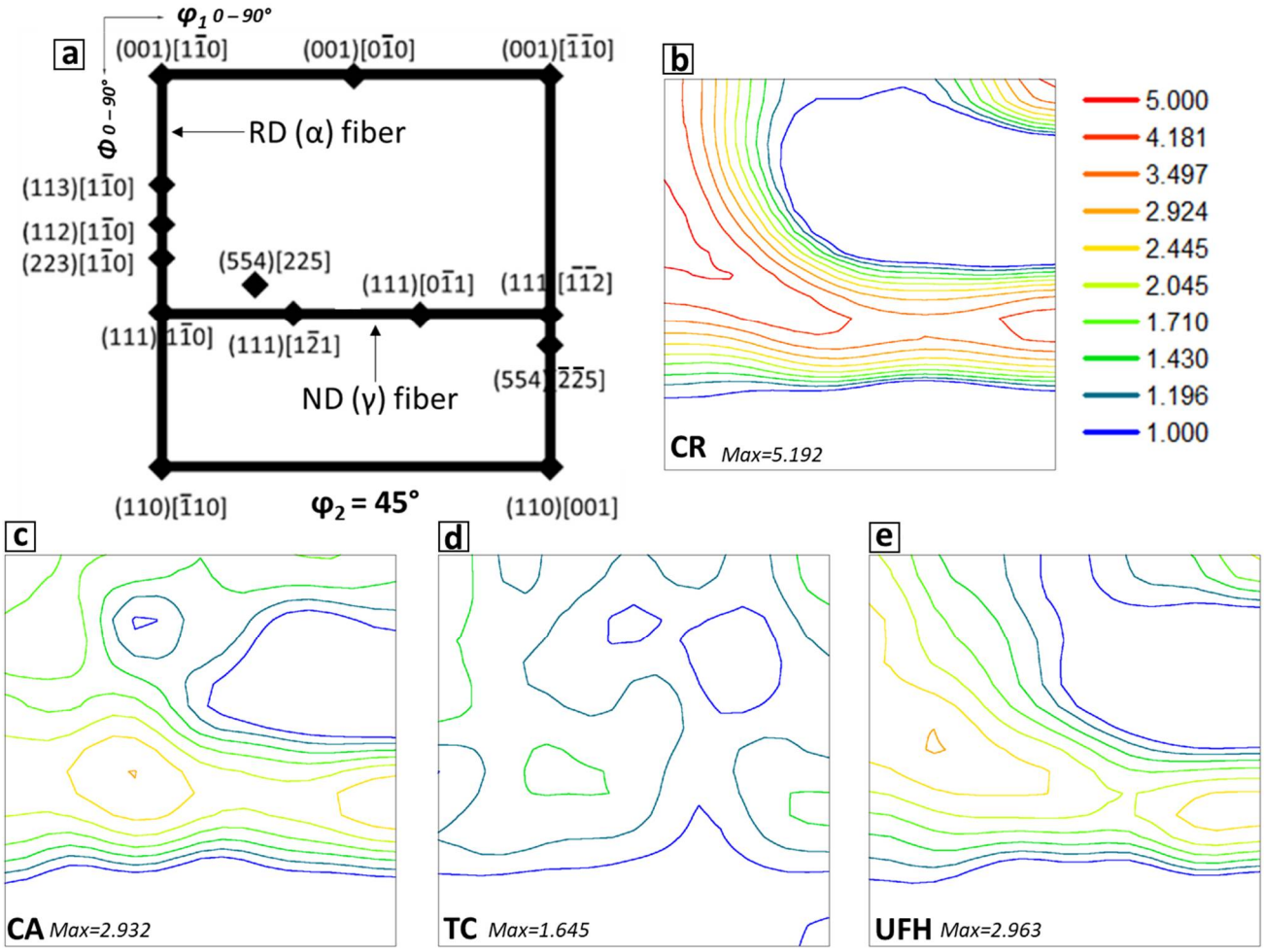

Figure 7. ODF at φ_2 = 45° section of the Euler space. (**a**) main texture components of rolled BCC crystals. (**b**) 70% cold-rolled material. (**c**) CA. (**d**) TC. (**e**) UFH. (Scanned area 22,500 μm^2).

3.3. Mechanical Properties

Tensile engineering stress–strain and strain hardening rate v/s true strain curves are shown in Figure 8a,b, respectively. Mechanical property values are summarized in Table 3. Bainitic steels produced in this study display continuous yielding and comparable values of ultimate tensile strength (σ_{UTS}). Yield strength (σ_{ys}) values of 895 MPa, 869 MPa and 862 MPa were measured for samples CA, TC and UFH, respectively. The obtained σ_{UTS} ranged from 1130 to 1135 MPa. Tensile testing, specifically the uniform (ε_u) and total (ε_{total}) elongation values, revealed a considerable difference in ductility for UFH with respect to samples CA and TC. In CA and TC steels, ε_u and ε_{total} are similar with values close to ≈0.15 and 0.25, respectively. The sample UFH shows an ε_u and a ε_{total} of 0.24 and 0.35, respectively. The reported difference in the elongation values represents an increment of 60% in ε_u and 40% in ε_{total} for the sample UFH with respect to CA and TC. Absorbed energy values of 251 MJ/m^3, 268 MJ/m^3 and 375 MJ/m^3 were determined for CA, TC and UFH, respectively.

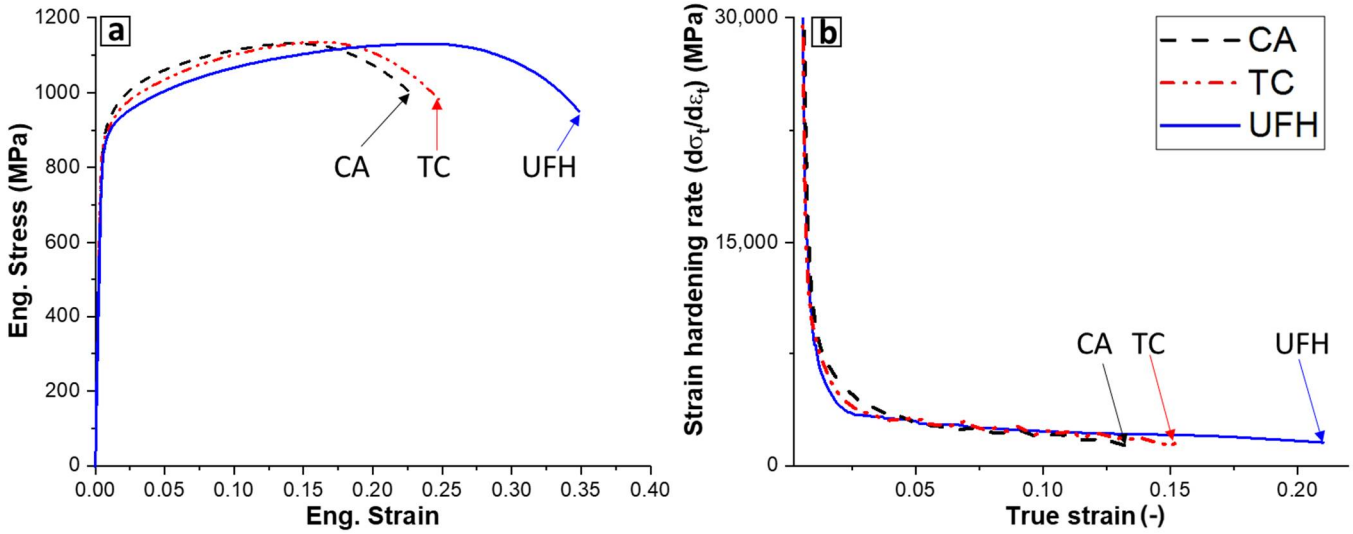

Figure 8. (**a**) Engineering stress-strain curves and (**b**) strain hardening rate v/s true strain curves.

Table 3. Mechanical properties (standard deviation).

Sample	σ_{ys}, MPa	σ_{UTS}, MPa	σ_{UTS}/σ_{ys}	ε_u	ε_{total}	Absorbed Energy, MJ/m^3
CA	895 (8)	1131 (2)	1.26 (0.01)	0.14 (0.001)	0.24 (0.005)	251 (6)
TC	869 (8)	1135 (7)	1.31 (0.003)	0.16 (0.003)	0.25 (0.006)	268 (4)
UFH	862 (13)	1130 (6)	1.31 (0.003)	0.24 (0.01)	0.35 (0.004)	375 (1)

The strain hardening behavior of the studied steels is presented in Figure 8b. Below a true strain of 0.05, sample CA displays the highest strain hardening rate and UFH the lowest one. In the true strain range from 0.05 to 0.11, all bainitic steels present a gradual decrease of the strain hardening rate, which is extended up to ≈0.21 for the UFH sample.

4. Discussion

Thermo-cycling and ultrafast heating produced microstructures finer than conventional annealing (Figures 5 and 6). The fine-sized PAGs and product microconstituents obtained via thermo-cycling are the results of multiple reverse transformations martensite-austenite in each cycle. Consecutive nucleation of austenite at prior parent austenite and martensitic grain boundaries [6,8], like blocks and packets, together with an increase in heating rate (10 °C/s to 30 °C/s) and 2 s of holding time, resulted in a measurable refining the grain size in the studied steel. At the same time, multiple reverse transformations randomized texture fibers of the initial material, and localized texture components of low intensity were developed (Figure 7d). Multiple variant selection, related to the transformation from austenite to martensite/bainite [36] (24 variants of the K-S orientation relationship), resulted in the low intensity (multiples of random distribution) observed for the heat-treated samples in comparison with the as-received material. According to this, multiple and subsequent steps of transformation martensite → austenite → martensite are responsible for the weaker texture observed for TC. On the other hand, the conventional annealed sample displays a texture with higher intensity on the {554}<225> and {111}<112> components, being similar to the crystallographic texture observed in recrystallized ferrite [45,46]. The low heating rate employed during conventional annealing (i.e., 10 °C/s) leads to the recrystallization of ferrite during heating, conducing to the transformation of grains with orientations that compose the RD fiber texture (such as {112}<110>) to grains with orientation close to {111}<112> and {554}<225> [45], which are the orientations observed after conventional annealing followed by austempering

(Figure 7c). Also, {111}<112> and {001}<011> orientations components can be obtained as results of transformation from parent austenite grains of brass orientation [47]. Large PAGs and bainitic blocks for CA are the result of the slow heating rate and soaking for 180 s at the annealing temperature, where the selected annealing parameters produce both, isochronal and isothermal austenitic grain growth.

The ODF of the UFH sample (Figure 7e) shows that the general characteristics of the BCC texture are almost the same compared with the as-received material (Figure 7b). This phenomenon can be explained in terms of the texture memory effect hypothesis [46] and similar results have been previously reported for different ultrafast heated steel grades, including Q&P steels [18–20,44]. In this work, evidence of austenite formation and its interaction with non-recrystallized ferrite ($F_{(Non\text{-}RX)}$) during the heating process is presented. Figure 9 shows selected $F_{(Non\text{-}RX)}$ grains in an intercritical annealed sample heated at 500 °C/s to 800 °C and quenched with no soaking time. A high density of dislocations is indirectly observed in the 1st neighbor kernel average misorientation maps exhibited in Figure 9a,b, proving that ferrite is in a non-recrystallized state during austenite formation. The ODF map presented in Figure 9c supports this observation.

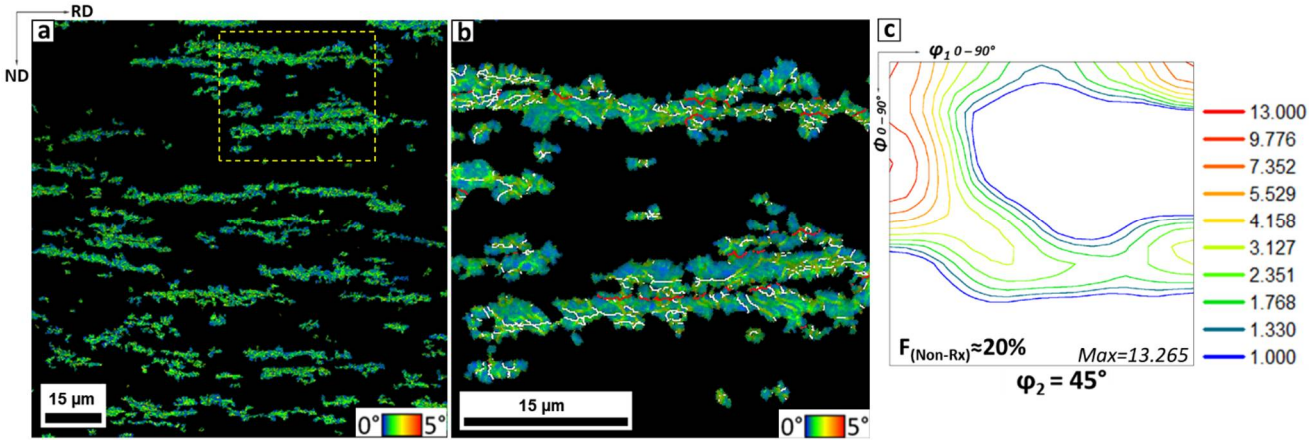

Figure 9. Non-recrystallized ferrite obtained in a sample heated at 500 °C/s to 800 °C followed by direct quenching: (**a**) 1st neighbour kernel average misorientation map. (**b**) Enlarged IQ-KAM map of the area enclosed by the dashed square in (**a**). White and red lines define boundaries with misorientation angles between 5–15° and 15–63°, respectively. (**c**) Orientation distribution function (scanned area 22,500 µm^2).

The ODF of the $F_{(Non\text{-}RX)}$ grains shows a convex curvature of the ND fiber and high intensity in the {113}<110> and {112}<110> rolling texture components. Texture characteristics of $F_{(Non\text{-}RX)}$ are restored after the transformation of $F_{(Non\text{-}RX)}$ → austenite → bainite giving rise to the crystallographic orientation observed for the UFH bainitic steel (Figure 7e), even after heating the sample above the A_{C3} temperature. Those non-recrystallized ferritic regions provide a high density of nucleation sites for austenite [48]. Additionally, the high heating rate and undissolved carbides can effectively suppress the austenitic grain growth upon heating [18,20], resulting in the fine-grained bainitic structure produced after ultrafast heating annealing and austempering.

It is important to note that the four-step thermo-cycling applied in this study, which includes heating up to a temperature range above A_{C3} followed by fast cooling, gives an equivalent grain refinement effect to the obtained through the UFH route, as presented in Figure 6b.

The microstructure produced after a predefined thermal treatment depends on the chemical and morphological characteristics of the parent austenite and subsequent thermal pathways. In this study, a fast-cooling rate of 160 °C/s was employed after the initial annealing step. This approach makes it possible to elucidate the characteristics of the parent austenite based on the microstructure obtained after cooling. Figure 10 shows the microstructure of the as-received ferritic–pearlitic steel (Figure 10a) together with samples

CA (Figure 10b) and UFH (Figure 10c) directly cooled to room temperature (the microstructure of TC is presented in Figure 4b). Clear differences are observed between CA and UFH. In the UFH steel, a banded microstructure that resembles the ferritic–pearlitic bands of the as-received cold-rolled material was obtained. The insert in Figure 10c shows that the darker areas in the optical micrograph are mainly composed of fine-grained ferrite, as it was presented previously in Figure 4c. Contrarily, even distribution of microconstituents was found in CA and TC. The influence of the prior annealing strategies on the produced microstructures is exemplified using schematic continuous cooling transformation diagrams (presented in Figure 10d,e).

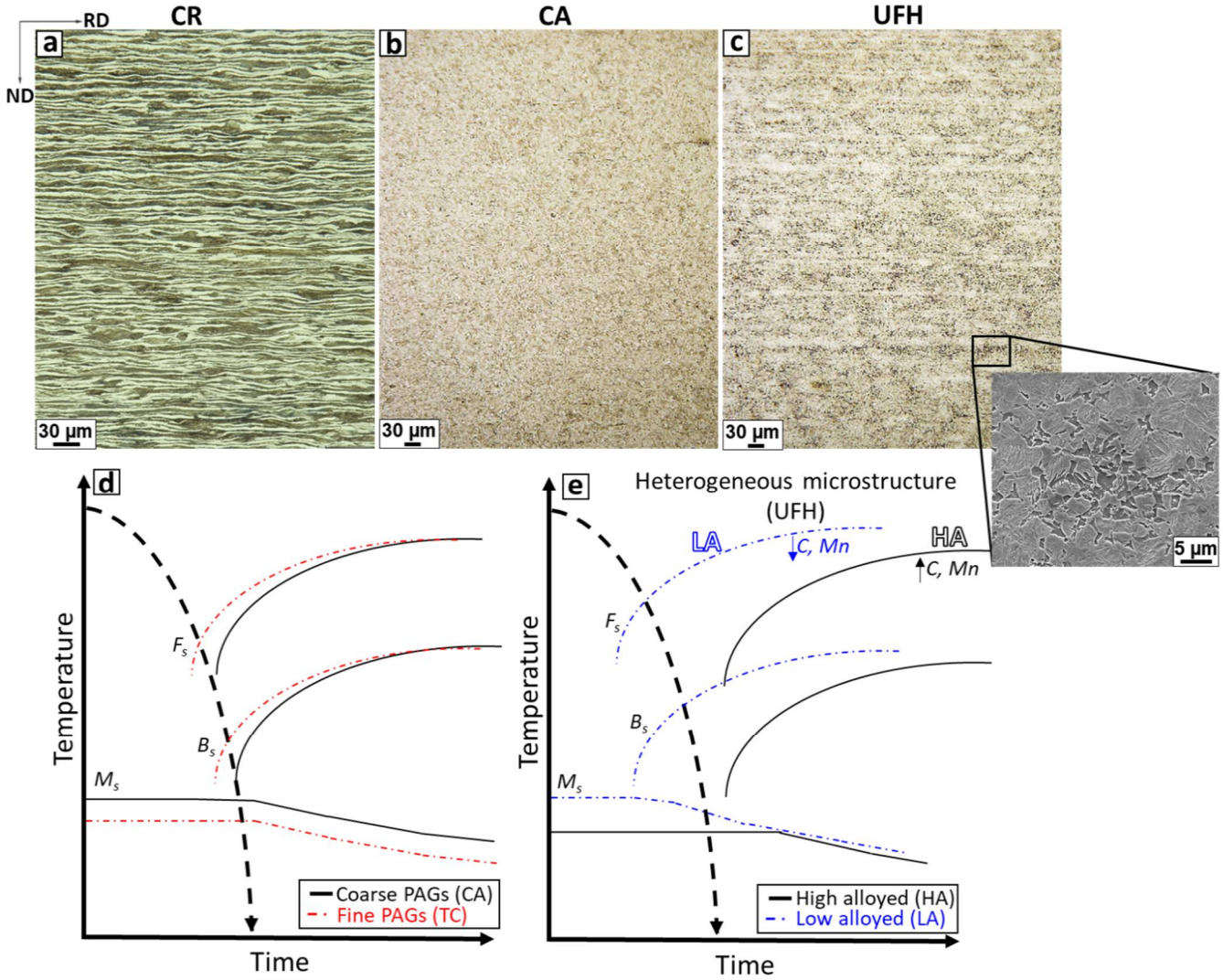

Figure 10. Optical micrographs for: (**a**) as-received material, (**b**) CA and (**c**) UFH samples. As a reference for the reader, the insert in (**c**) shows an enlarged micrograph of the heterogeneous microstructure obtained within the martensitic bands for the UFH sample. (**d**) Schematic CCT diagrams presenting the influence of the PAG size on phase transformations for CA and TC samples. (**e**) Chemical gradients in parent austenite produced via ultrafast heating annealing led to different kinetics of phase transformation (local CCT diagrams) for the UFH sample. The banded microstructure produced after UFH is inherited from the initial cold-rolled material, where LA (ferritic) and HA (pearlitic) are low alloyed and high alloyed regions, respectively.

Conventional annealing produces a homogeneous parent austenite phase of a rather large grain size if it is compared to the grain size distributions of TC and UFH. After cooling, a ferrite fraction lower than 1% was obtained for CA, with ferritic grains nucleated at prior austenite grain boundaries. The decrease in the PAGs size by thermo-cycling

annealing led to a higher amount of effective nucleation points [7], resulting in an increased number of ferritic grains obtained after cooling. The decrease in the M_S temperature is also related to the smaller PAGs produced after TC, and this phenomenon has been reported and discussed elsewhere [2,13]. On the other hand, the banded microstructure obtained after ultrafast heating and cooling is linked to the chemical heterogeneity of the parent austenite. The homogenization of manganese and carbon might be constrained during the ultrafast heating annealing [16,30,49]. This is a reason to obtain compositional gradients in the parent austenite, with regions of high and low solute concentration at prior pearlitic (high alloyed region, HA) and deformed ferritic bands (low alloyed region, LA), respectively [50,51]. During the initial stages of nucleation, austenite forms preferentially at prior pearlitic regions [26]. Additionally, austenite can also nucleate at ferrite–ferrite boundaries. Nevertheless, the growth of those nuclei will be controlled through carbon diffusion from the carbon-rich areas [48,52]. Another transformation mechanism that could operate upon fast heating is the massive growth of austenite from proeutectoid ferrite at the last stage of austenite formation [26,27]. As the homogenization of carbon and the alloying elements is likely restricted by the high heating rate and short soaking time employed (<0.3 s), low and high solute regions in parent austenite will transform following different kinetics of phase transformations, as presented in Figure 10e. The results suggest that LA regions decompose to a mixture of ferrite and possible bainite, while prior HA regions are transformed mainly to martensite due to the inhomogeneous distribution of alloying elements in austenite. These results concur with those reported for lean alloy steels subjected to ultrafast heating and fast cooling [15,49,53–55].

According to the mechanical properties, the decrease in the grain size attained via thermo-cycling treatment resulted in equivalent σ_{UTS} and elongation values to the obtained in CA. These observations are in line with previous results in the influence of PAG size and the related mechanical performance of martensitic steels by Hanamura et al. [2]. The results suggest that the decrease in the average bainitic block length from 5.3 μm (CA) to 3.5 μm (TC) and 3.4 μm (UFH) does not play a major role on the overall mechanical behavior of the studied steels. Instead, the combination of ultrafast heating and austempering produced higher uniform and total elongation, resulting in an enhanced strength-ductility balance and superior capacity of energy absorption during tensile testing.

The distribution of microconstituents and corresponding mechanical properties obtained after austempering are summarized in Figure 11. The results indicate that the σ_{UTS} values are insensitive to the processing history and microstructure. This observation agrees with the findings reported by Kumar et al. [56], where a saturation of the strength level was obtained in dual-phase steels with bainite or martensite content higher than 60%.

The resulting mechanical properties obtained via the combination of UFH and austempering agree well with previous findings reported for UFH-Q&P steels [18,25], for which a promising compromise between total elongation and high strength level was found through the formation of ferrite-containing multiphase microstructures. Those results [18,25] suggested that the presence of ferrite does not affect the strength level but effectively contributes towards improving the tensile strain capacity of UFH steels.

In multiphase steels, the fraction, strength, distribution and size of each microstructural constituent define the mechanical behavior [57,58]. The strain hardening is also influenced by stress partitioning and strain accommodation between phases during deformation [59,60]. Additionally, the mechanical stability of retained austenite and its interaction with the surrounding microconstituents play a fundamental role on the strain hardening rate of TRIP-aided steels [59,61,62].

Noticeable differences in the strain hardening rates of the studied steels are observed at the initial stages of deformation, before reaching a strain value of 0.05 (Figure 8b). In an attempt to elucidate the potential effect of the microstructure on the mechanical behavior, the measured strain hardening rates were analyzed by using the modified Crussard-Jaoul analysis [63,64]. Figure 12 shows representative plots of $\ln(d\sigma_t/d\varepsilon_t)$ vs. $\ln(\sigma_t)$ for the

studied steels. Three different stages (s_{I-III}) of strain hardening are observed; true stress (ε_t) and true strain (σ_t) values at the transition of each stage are indicated in parenthesis.

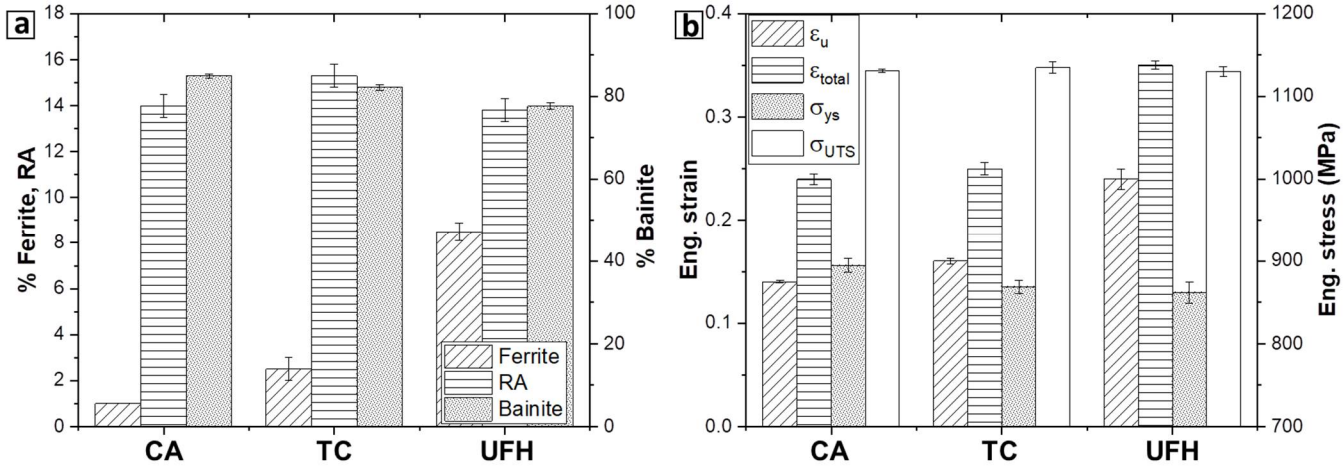

Figure 11. (**a**) Distribution of microconstituents in austempered samples (the amount of martensite is lower than 1% for all samples). RA: retained austenite. (**b**) Summary of the mechanical properties measured via uniaxial tensile testing. ε_U: uniform elongation; ε_{total}: total elongation; σ_{ys}: 0.2% yield strength; σ_{UTS}: ultimate tensile strength.

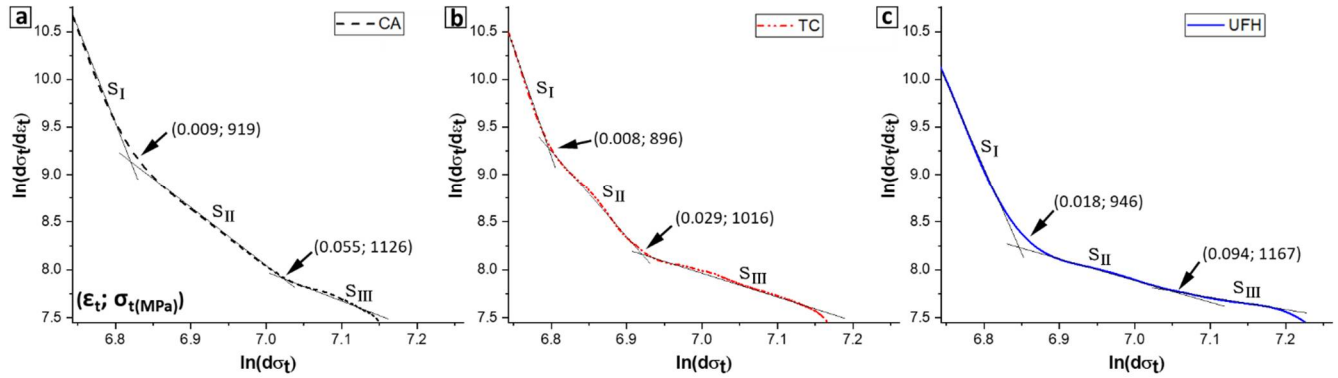

Figure 12. Strain hardening behavior plotted according to the modified C-J analysis in samples (**a**) CA, (**b**) TC and (**c**) UFH. Values indicated in parenthesis at the inflection points of the strain hardening curves correspond to the true strain and true stress, respectively (true strain; true stress).

During stage 1 (s_I), initial yielding and dislocation accumulation in bainitic regions lead to high strain hardening rates for samples CA and TC. At this stage, the accumulation of mobile dislocations at regions near to retained austenite grains takes place [65]. It is expected that the retained austenite grains that compose M/γ islands are among the first to transform due to the constraining effect on strain distribution and locally higher stress levels that arise in the regions surrounding the initial martensitic zones [66]. Retained austenite grains of low mechanical stability might also transform to martensite in this stage. Stage 1 is prolonged to higher levels of stress and strain in the UFH sample due to the homogeneous deformation of soft ferritic grains, which resulted in the lowest strain hardening rate observed at the early stages of deformation [64,67]. In stage 2 (s_{II}), retained austenite grains continuously transform to martensite due to the accumulation of strain. This transformation attenuates the strain hardening rate decreasing by inhibiting the dislocation glide process in regions where newly martensite grains were formed [65,68]. The higher strain hardening rate at the initial stages of deformation for CA and TC samples might be also influenced by a fast rate of austenite transformation upon straining. The C-J plots indicate that most of the austenite transformation proceeds quickly at low strain levels in samples CA and TC (before reaching the stress level corresponding to stage 3). This observation agrees

with the results for the kinetics of austenite transformation upon straining in low alloy steels [69–71]. Instead, variations of strain hardening in the UFH sample suggest that austenite transformation is prolonged to higher levels of strain and proceeds at a slower rate than in CA and TC. This is an indication for retained austenite of higher mechanical stability, resulting in improved ductility and energy absorption capacity [70,71]. Liu et al. [16] pointed out that the chemical heterogeneities in retained austenite, generated during ultrafast heating experiments, may play a role on the mechanical behavior of multiphase ultrafast heated steels. The higher carbon and manganese concentration in austenite formed at prior pearlitic colonies may account to improve the mechanical stability of the RA grains [61,62], enhancing the ductility of the UFH steel.

During stage 3 (s_{III}), the deformation of bainite and ferrite continues. Retained austenite grains of higher mechanical stability also transform during this stage. The newly formed martensite islands act like hard particles, producing the redistribution of plastic deformation towards bainitic and ferritic constituents [68].

In addition to this analysis, it should be mentioned that the formation of the heterogeneously banded microstructure produced via UFH might lead to strain/stress gradients between ferrite, bainite and retained austenite (which transforms to martensite upon straining), producing a synergic effect that conduced to the enhancement of ductility without decreasing the strength level, as reported in Refs. [72–74]. Ryu et al. demonstrated that the strain partitioning between microconstituents in low alloy steels drastically influences the stability of retained austenite [75], and this factor could be related to the higher mechanical stability indirectly evaluated for the RA grains in the UFH sample. According to the discussed results and reported mechanical properties for multiphase UFH-Q&P steels [18,25], ferrite grains could effectively contribute to the ductility by decreasing the strain localization, improving the retained austenite stability.

However, the exact quantitative analyses of the influence of the spatial distribution of microconstituents and their contribution to the mechanical behavior, coupled with the evaluation of kinetics and hardening related to the austenite → martensite transformation upon straining remain open for further investigation.

5. Conclusions

In this study, the influence of thermo-cycling and ultrafast heating annealing strategies on microstructure-mechanical properties of austempered steels were evaluated and compared with a steel grade produced via a conventional annealing route. The following conclusions are addressed from the obtained results:

1. Four-step thermo-cycling and ultrafast heating above the A_{C3} led to finer microstructures than conventional annealing. Retained austenite grain distributions were not greatly influenced by the prior annealing treatment.
2. The microstructural refinement attained via thermo-cycling does not show a significant influence on the mechanical response for the studied steels.
3. Ultrafast heating above the A_{C3} followed by fast cooling to room temperature retains a banded microstructure mainly composed of martensite and ferrite. The banded characteristics of the heat-treated material are similar to the observed in the as-received ferritic–pearlitic steel. Microstructural analysis suggested that the banded microstructure developed after heat treatment arises from local chemical heterogeneities in the parent austenite due to insufficient time for diffusion of alloying elements during the UFH process.
4. In contrast to the conventional annealed sample, the grain refined-heterogeneous microstructure produced via a combination of UFH and austempering led to an increase of 40% in total elongation and 50% in energy absorbed measured under uniaxial strain to fracture.
5. The enhancement of ductility of the UFH-bainitic steel is reached without sacrificing the strength level. The obtained results suggest that the formation of heterogeneous

microstructures via ultrafast heating annealing has a greater influence on the mechanical response than the attained level of grain refinement.

Author Contributions: Conceptualization, E.H.-D., F.C.-C., T.R.-Y. and R.H.P.; methodology, E.H.-D. and L.C.; software, E.H.-D. and L.C.; investigation, E.H.-D.; resources, R.H.P.; writing—original draft preparation, E.H.-D.; writing—review and editing, L.C., F.C.-C., T.R.-Y. and R.H.P.; supervision, F.C.-C. and R.H.P.; funding acquisition, E.H.-D., F.C.-C. and R.H.P. All authors have read and agreed to the published version of the manuscript.

Funding: This research was funded by National Agency for Research and Development (ANID-Chile)/Doctorado Nacional/2017-21171319 (E.H.D.) and Project No. 11170104 (F.C.C.).

Institutional Review Board Statement: Not applicable.

Informed Consent Statement: Not applicable.

Data Availability Statement: Not applicable.

Acknowledgments: L. Corallo acknowledges the support of Research Foundation Flanders-FWO, application number 1SC5619N.

Conflicts of Interest: The authors declare no conflict of interest.

References

1. Morrison, W. Effect of grain size on the stress-strain relationship in low-carbon steel. *Trans. ASM* **1966**, *59*, 824–846.
2. Hanamura, T.; Torizuka, S.; Tamura, S.; Enokida, S.; Takech, H. *Effect of Austenite Grain Size on the Mechanical Properties in Air-Cooled 0.1c-5Mn Martensitic Steel*; Trans Tech Publications Ltd.: Stafa-Zurich, Switzerland, 2014; Volume 783–786, pp. 1027–1032. [CrossRef]
3. Tomita, Y.; Okabayashi, K. Heat treatment for improvement in lower temperature mechanical properties of 0.40 pct C-Cr-Mo ultrahigh strength steel. *Metall. Trans. A* **1983**, *14*, 2387–2393. [CrossRef]
4. Garcia-Mateo, C.; Caballero, F.G.; Sourmail, T.; Kuntz, M.; Cornide, J.; Smanio, V.; Elvira, R. Tensile behaviour of a nanocrystalline bainitic steel containing 3wt% silicon. *Mater. Sci. Eng. A* **2012**, *549*, 185–192. [CrossRef]
5. Yokota, T.; Mateo, C.G.; Bhadeshia, H.K.D.H. Formation of nanostmctured steels by phase transformation. *Scr. Mater.* **2004**, *51*, 767–770. [CrossRef]
6. Furuhara, T.; Kikumoto, K.; Saito, H.; Sekine, T.; Ogawa, T.; Morito, S.; Maki, T. Phase transformation from fine-grained austenite. *ISIJ Int.* **2008**, *48*, 1038–1045. [CrossRef]
7. Grange, R.A. Strengthening steel by austenite grain refinemet. *Trans. ASM* **1966**, *59*, 26–48.
8. Grange, R.A. The rapid heat treatment of steel. *Metall. Trans.* **1971**, *2*, 65–78. [CrossRef]
9. Baker, T.N. Microalloyed steels Microalloyed steels. *Ironmak. Steelmak.* **2016**, *43*, 264–307. [CrossRef]
10. Buchmayr, B. Thermomechanical Treatment of Steels—A Real Disruptive Technology Since Decades. *Steel Res. Int.* **2017**, *87*, 1–14. [CrossRef]
11. Zhao, J.; Jiang, Z. Thermomechanical processing of advanced high strength steels. *Prog. Mater. Sci.* **2018**, *94*, 174–242. [CrossRef]
12. Dai, Z.; Chen, H.; Ding, R.; Lu, Q.; Zhang, C.; Yang, Z.; Van Der Zwaag, S. Fundamentals and application of solid-state phase transformations for advanced high strength steels containing metastable retained austenite. *Mater. Sci. Eng. R* **2021**, *143*, 100590. [CrossRef]
13. Celada-Casero, C.; Sietsma, J.; Santofimia, M.J. The role of the austenite grain size in the martensitic transformation in low carbon steels. *Mater. Des.* **2019**, *167*, 107625. [CrossRef]
14. Matlock, D.K.; Kang, S.; De Moor, E.; Speer, J.G. Applications of rapid thermal processing to advanced high strength sheet steel developments. *Mater. Charact.* **2020**, *166*, 110397. [CrossRef]
15. Banis, A.; Bouzouni, M.; Gavalas, E.; Papaefthymiou, S. The formation of a mixed martensitic/bainitic microstructure and the retainment of austenite in a medium-carbon steel during ultra-fast heating. *Mater. Today Commun.* **2021**, *26*, 101994. [CrossRef]
16. Liu, G.; Li, T.; Yang, Z.; Zhang, C.; Li, J.; Chen, H. On the role of chemical heterogeneity in phase transformations and mechanical behavior of flash annealed quenching & partitioning steels. *Acta Mater.* **2020**, *201*, 266–277. [CrossRef]
17. Cola, G.M. Replacing hot stamped, boron, and DP1000 with "room temperature formable" Flash®® Bainite 1500 advanced high strength steel. In Proceedings of the 28th Heat Treating Society Conference, (HEAT Treating 2015), Detroit, MI, USA, 20–22 October 2015; pp. 21–28.
18. De Knijf, D.; Puype, A.; Föjer, C.; Petrov, R. The influence of ultra-fast annealing prior to quenching and partitioning on the microstructure and mechanical properties. *Mater. Sci. Eng. A* **2015**, *627*, 182–190. [CrossRef]
19. Da Costa-Reis, A.; Bracke, L.; Petrov, R.; Kaluba, W.J.; Kestens, L. Grain Refinement and Texture Change in Interstitial Free Steels after Severe Rolling and Ultra-short Annealing. *ISIJ Int.* **2003**, *43*, 1260–1267. [CrossRef]

20. Petrov, R.H.; Sidor, J.; Kestens, L.A.I. Texture formation in high strength low alloy steel reheated with ultrafast heating rates. *Mater. Sci. Forum* **2012**, *702–703*, 798–801. [CrossRef]
21. Petrov, R.; Kestens, L.; Kaluba, W.; Houbaert, Y. Recrystallization and austenite formation in a cold rolled TRIP steel during ultra fast heating. *Steel Grips* **2003**, *289–294*, 221–225.
22. Hudd, R.C.; Lyons, L.K.; De Paepe, A.; Stolz, C.; Collins, J. *The Ultra Rapid Heat Treatment of Low Carbon Strip*; European Commission Project Contract No 7210-MB/818/203/819; Office for Official Publications of the European Communities: Luxembourg, 1998.
23. Griffay, G.; Anderhuber, M.; Klinkenberg, P.; Tusset, V. *New Continuous Annealing Technology with High-Speed Induction Heating Followed by Ultra-Fast Cooling*; European Commission Project Contract No 7210-PR/026; Office for Official Publications of the European Communities: Luxembourg, 2002.
24. Hernandez-Duran, E.I.; Corallo, L.; Ros-Yanez, T.; Castro-Cerda, F.M.; Petrov, R.H. Influence of Mo-Nb-Ti additions and peak annealing temperature on the microstructure and mechanical properties of low alloy steels after ultrafast heating process. *Mater. Sci. Eng. A* **2021**, *808*, 140928. [CrossRef]
25. Dai, J.; Meng, Q.; Zheng, H. An innovative pathway to produce high-performance quenching and partitioning steel through ultra-fast full austenitization annealing. *Mater. Today Commun.* **2020**, *25*, 101272. [CrossRef]
26. Speich, G.; Szirmae, A. Formation of Austenite from Ferrite and Ferrite-Carbide Aggregates. *Trans. Metall. Soc. AIME* **1969**, *245*, 1063–1074.
27. Castro Cerda, F.M.; Sabirov, I.; Goulas, C.; Sietsma, J.; Monsalve, A.; Petrov, R.H. Austenite formation in 0.2% C and 0.45% C steels under conventional and ultrafast heating. *Mater. Des.* **2017**, *116*, 448–460. [CrossRef]
28. Thomas, L.S.; Matlock, D.K. Formation of Banded Microstructures with Rapid Intercritical Annealing of Cold-Rolled Sheet Steel. *Metall. Mater. Trans. A Phys. Metall. Mater. Sci.* **2018**, *49*, 4456–4473. [CrossRef]
29. Mishra, S.; DebRoy, T. Non-isothermal grain growth in metals and alloys. *Mater. Sci. Technol.* **2006**, *22*, 253–278. [CrossRef]
30. Liu, G.; Dai, Z.; Yang, Z.; Zhang, C.; Li, J.; Chen, H. Kinetic transitions and Mn partitioning during austenite growth from a mixture of partitioned cementite and ferrite: Role of heating rate. *J. Mater. Sci. Technol.* **2020**, *49*, 70–80. [CrossRef]
31. Thomas, L. Effect of heating rate on intercritical annealing of low-carbon cold-rolled steel. Ph.D. Thesis, Colorado School of Mines, Golden, CO, USA, 2015.
32. Azizi-Alizamini, H.; Militzer, M.; Poole, W.J. Austenite formation in plain low-carbon steels. *Metall. Mater. Trans. A Phys. Metall. Mater. Sci.* **2011**, *42*, 1544–1557. [CrossRef]
33. Kaar, S.; Steineder, K.; Schneider, R.; Krizan, D.; Sommitsch, C. New Ms-formula for exact microstructural prediction of modern 3rd generation AHSS chemistries. *Scr. Mater.* **2021**, *200*, 113923. [CrossRef]
34. Matas, S.; Hehemann, R.F. The Structure of Bainite in Hypoeutectoid Steels. *Trans. Metall. Soc. AIME* **1961**, *221*, 179–185.
35. Pierce, D.T.; Coughlin, D.R.; Williamson, D.L.; Clarke, K.D.; Clarke, A.J.; Speer, J.G. Characterization of transition carbides in quench and partitioned steel microstructures by Mossbauer spectroscopy and complementary techniques. *Acta Mater.* **2015**, *90*, 417–430. [CrossRef]
36. Takayama, N.; Miyamoto, G.; Furuhara, T. Effects of transformation temperature on variant pairing of bainitic ferrite in low carbon steel. *Acta Mater.* **2012**, *60*, 2387–2396. [CrossRef]
37. Gomes de Araujo, E.; Pirgazi, H.; Sanjari, M.; Mohammadi, M.; Kestens, L.A.I. Automated reconstruction of parent austenite phase based on the optimum orientation relationship. *J. Appl. Crystallogr.* **2021**, *54*, 569–579. [CrossRef]
38. Aaronson, H.I. The proeutectoid ferrite and the proeutectoid cementite reactions. In Proceedings of the the Decomposition of Austenite by Diffusional Processes, Philadelphia, PA, USA, 19 October 1960; pp. 387–546.
39. Navarro-López, A.; Hidalgo, J.; Sietsma, J.; Santofimia, M.J. Characterization of bainitic/martensitic structures formed in isothermal treatments below the Ms temperature. *Mater. Charact.* **2017**, *128*, 248–256. [CrossRef]
40. Hofer, C.; Bliznuk, V.; Verdiere, A.; Petrov, R.; Winkelhofer, F.; Clemens, H.; Primig, S. Correlative microscopy of a carbide-free bainitic steel. *Micron* **2016**, *81*, 1–7. [CrossRef]
41. Scott, C.P.; Drillet, J. A study of the carbon distribution in retained austenite. *Scr. Mater.* **2007**, *56*, 489–492. [CrossRef]
42. Caballero, F.G.; Miller, M.; Garcia-Mateo, C. Slow Bainite: An Opportunity to Determine the Carbon Content of the Bainitic Ferrite during Growth Francisca G. Caballero. *Solid State Phenom.* **2011**, *174*, 111–116. [CrossRef]
43. Clarke, A.J.; Speer, J.G.; Miller, M.K.; Hackenberg, R.E.; Edmonds, D.V.; Matlock, D.K.; Rizzo, F.C.; Clarke, K.D.; De Moor, E. Carbon partitioning to austenite from martensite or bainite during the quench and partition (Q&P) process: A critical assessment. *Acta Mater.* **2008**, *56*, 16–22. [CrossRef]
44. Hernandez-Duran, E.I.; Ros-Yanez, T.; Castro-Cerda, F.M.; Petrov, R.H. The influence of the heating rate on the microstructure and mechanical properties of a peak annealed quenched and partitioned steel. *Mater. Sci. Eng. A* **2020**, *797*, 140061. [CrossRef]
45. Hoelscher, M.; Raabe, D.; Lucke, K. Rolling and recrystallization texture in BCC steels. *Steel Res.* **1991**, *62*, 567–575. [CrossRef]
46. Yoshinaga, N.; Inoue, H.; Kawasaki, K.; Kestens, L.; De Cooman, B.C. Factors affecting texture memory appearing through $\alpha \rightarrow \gamma \rightarrow \alpha$ transformation in IF steels. *Mater. Trans.* **2007**, *48*, 2036–2042. [CrossRef]
47. Butrón-Guillén, M.P.; Jonas, J.J.; Ray, R.K. Effect of austenite pancaking on texture formation in a plain carbon and A Nb microalloyed steel. *Acta Metall. Mater.* **1994**, *42*, 3615–3627. [CrossRef]
48. Zheng, C.; Raabe, D. Interaction between recrystallization and phase transformation during intercritical annealing in a cold-rolled dual-phase steel: A cellular automaton model. *Acta Mater.* **2013**, *61*, 5504–5517. [CrossRef]

49. Albutt, K.; Garber, S. Effect of heating rate on the elevation of the critical temperatures of low-carbon mild steel. *J. Iron Steel Inst.* **1966**, *204*, 1217–1222.
50. Verhoeven, J.D. Review of microsegregation induced banding phenomena in steels. *J. Mater. Eng. Perform.* **2000**, *9*, 286–296. [CrossRef]
51. Grange, R.A. Effect of microstructural banding in steel. *Metall. Trans.* **1971**, *2*, 417–426. [CrossRef]
52. Savran, V.I.; Leeuwen, Y.; Hanlon, D.N.; Kwakernaak, C.; Sloof, W.G.; Sietsma, J. Microstructural features of austenite formation in C35 and C45 alloys. *Metall. Mater. Trans. A Phys. Metall. Mater. Sci.* **2007**, *38*, 946–955. [CrossRef]
53. Lolla, T.; Cola, G.; Narayanan, B.; Alexandrov, B.; Babu, S.S. Development of rapid heating and cooling (flash processing) process to produce advanced high strength steel microstructures. *Mater. Sci. Technol.* **2011**, *27*, 863–875. [CrossRef]
54. Sackl, S.; Zuber, M.; Clemens, H.; Primig, S. Induction Tempering vs. Conventional Tempering of a Heat-Treatable Steel. *Metall. Mater. Trans. A* **2016**, *47*, 3694–3702. [CrossRef]
55. Pedraza, J.; Landa-Mejia, R.; Garcia-Rincon, O.; Garcia, I. The Effect of Rapid Heating and Fast Cooling on the Transformation Behavior and Mechanical Properties of an Advanced High Strength Steel (AHSS). *Metals* **2019**, *545*, 1–12.
56. Kumar, A.; Singh, S.B.; Ray, K.K. Influence of bainite/martensite-content on the tensile properties of low carbon dual-phase steels. *Mater. Sci. Eng. A* **2008**, *474*, 270–282. [CrossRef]
57. Ismail, K.; Perlade, A.; Jacques, P.J.; Pardoen, T.; Brassart, L. Impact of second phase morphology and orientation on the plastic behavior of dual-phase steels. *Int. J. Plast.* **2019**, *118*, 130–146. [CrossRef]
58. Bhattacharyya, A.; Sakaki, T.; Weng, G.J. The Influence of Martensite Shape, Concentration, and Phase Transformation Strain on the Deformation Behavior of Stable Dual-Phase Steels. *Metall. Trans. A* **1993**, *24*, 301–314. [CrossRef]
59. Ennis, B.L.; Jimenez-melero, E.; Atzema, E.H.; Krugla, M. Metastable austenite driven work-hardening behaviour in a TRIP-assisted dual phase steel. *Int. J. Plast.* **2017**, *88*, 126–139. [CrossRef]
60. Calcagnotto, M.; Ponge, D.; Demir, E.; Raabe, D. Orientation gradients and geometrically necessary dislocations in ultrafine grained dual-phase steels studied by 2D and 3D EBSD. *Mater. Sci. Eng. A* **2010**, *527*, 2738–2746. [CrossRef]
61. Jimenez-Melero, E.; van Dijk, N.H.; Zhao, L.; Sietsma, J.; Wright, J.P.; Van Der Zwaag, S. In situ synchrotron study on the interplay between martensite formation, texture evolution and load partitioning in low-alloyed TRIP steels. *Mater. Sci. Eng. A* **2011**, *528*, 6407–6416. [CrossRef]
62. Ebner, S.; Schnitzer, R.; Maawad, E.; Suppan, C.; Hofer, C. Influence of partitioning parameters on the mechanical stability of austenite in a Q&P steel: A comparative in-situ study. *Materialia* **2021**, *15*, 101033. [CrossRef]
63. Tomita, Y.; Okabayashi, K. Tensile Stress-Strain Analysis of Cold Worked Metals and Steels and Dual-Phase Steels. *Metall. Trans. A* **1985**, *16*, 865–872. [CrossRef]
64. Soliman, M.; Palkowski, H. Strain Hardening Dependence on the Structure in Dual-Phase Steels. *Steel Res. Int.* **2021**, *92*, 1–15. [CrossRef]
65. Alharbi, F.; Gazder, A.A.; Kostryzhev, A.; De Cooman, B.C.; Pereloma, E.V. The effect of processing parameters on the microstructure and mechanical properties of low-Si transformation-induced plasticity steels. *J. Mater. Sci.* **2014**, *49*, 2960–2974. [CrossRef]
66. De Knijf, D.; Petrov, R.; Föjer, C.; Kestens, L.A.I. Effect of fresh martensite on the stability of retained austenite in quenching and partitioning steel. *Mater. Sci. Eng. A* **2014**, *615*, 107–115. [CrossRef]
67. Movahed, P.; Kolahgar, S.; Marashi, S.P.H.; Pouranvari, M.; Parvin, N. The effect of intercritical heat treatment temperature on the tensile properties and work hardening behavior of ferrite—Martensite dual phase steel sheets. *Mater. Sci. Eng. A* **2009**, *518*, 1–6. [CrossRef]
68. Timokhina, I.B.; Hodgson, P.D.; Pereloma, E. V Transmission Electron Microscopy Characterization of the Bake-Hardening Behavior of Transformation-Induced Plasticity and Dual-Phase Steels. *Metall. Mater. Trans. A* **2007**, *38*, 2442–2454. [CrossRef]
69. Polatidis, E.; Haidemenopoulos, G.N.; Krizan, D.; Aravas, N.; Panzner, T.; Papadioti, I.; Casati, N.; Van Petegem, S.; Van Swygenhoven, H. The effect of stress triaxiality on the phase transformation in transformation induced plasticity steels: Experimental investigation and modelling the transformation kinetics. *Mater. Sci. Eng. A* **2021**, *800*, 1–10. [CrossRef]
70. Pereloma, E.; Gazder, A.; Timokhina, I. Retained Austenite: Transformation-Induced Plasticity. *Encycl. Iron. Steel. Their Alloy.* **2016**, 3088–3103. [CrossRef]
71. Sugimoto, K.; Kobayashi, M.; Hashimoto, S. Ductility and Strain-Induced Transformation in a High-Strength Transformation-Induced Plasticity-Aided Dual-Phase Steel. *Metall. Trans. A* **1992**, *23*, 3085–3091. [CrossRef]
72. Lyu, H.; Hamid, M.; Ruimi, A.; Zbib, H.M. Stress/strain gradient plasticity model for size effects in heterogeneous nano-microstructures. *Int. J. Plast.* **2017**, *97*, 46–63. [CrossRef]
73. Hassan, S.F.; Al-Wadei, H. Heterogeneous Microstructure of Low-Carbon Microalloyed Steel and Mechanical Properties. *J. Mater. Eng. Perform.* **2020**, *29*, 7045–7051. [CrossRef]
74. Wu, X.; Zhu, Y. Heterogeneous materials: A new class of materials with unprecedented mechanical properties. *Mater. Res. Lett.* **2017**, *5*, 527–532. [CrossRef]
75. Ryu, J.H.; Kim, D.; Kim, S.; Bhadeshia, H.K.D.H. Strain partitioning and mechanical stability of retained austenite. *Scr. Mater.* **2010**, *63*, 297–299. [CrossRef]